Atmos. Chem. Phys. Discuss., 11, 12805–12848, 2011
www.atmos-chem-phys-discuss.net/11/12805/2011/
doi:10.5194/acpd-11-12805-2011

Atmospheric Chemistry and Physics Discussions

Three-dimensional variations of atmospheric CO_2: aircraft measurements and multi-transport model simulations

Y. Niwa[1], P. K. Patra[2], Y. Sawa[1], T. Machida[3], H. Matsueda[1], D. Belikov[3], T. Maki[1], M. Ikegami[4], R. Imasu[5], S. Maksyutov[3], T. Oda[3], M. Satoh[5,2], and M. Takigawa[2]

[1]Geochemical Research Department, Meteorological Research Institute, Tsukuba, Japan
[2]Research Institute for Global Change, Japan Agency for Marine–Earth Science and Technology, Yokohama, Japan
[3]Center for Global Environmental Research, National Institute for Environmental Studies, Tsukuba, Japan
[4]Japan Meteorological Agency, Tokyo, Japan
[5]Atmosphere and Ocean Research Institute, The University of Tokyo, Kashiwa, Japan

Received: 8 April 2011 – Accepted: 17 April 2011 – Published: 27 April 2011

Correspondence to: Y. Niwa (yniwa@mri-jma.go.jp)

Published by Copernicus Publications on behalf of the European Geosciences Union.

Abstract

Numerical simulation and validation of three-dimensional structure of atmospheric carbon dioxide (CO_2) is necessary for quantification of transport model uncertainty and its role on surface flux estimation by inverse modeling. Simulations of atmospheric CO_2 were performed using four transport models and two sets of surface fluxes compared with an aircraft measurement dataset of Comprehensive Observation Network for Trace gases by AIrLiner (CONTRAIL), covering various latitudes, longitudes, and heights. Under this transport model intercomparison project, spatiotemporal variations of CO_2 concentration for 2006–2007 were analyzed with a three-dimensional perspective. Results show that the models reasonably simulated vertical profiles and seasonal variations not only over northern latitude areas but also over the tropics and southern latitudes. From CONTRAIL measurements and model simulations, intrusion of northern CO_2 in to the Southern Hemisphere, through the upper troposphere, was confirmed. Furthermore, models well simulated the vertical propagation of seasonal variation in the northern free-troposphere. However, significant model–observation discrepancies were found in Asian regions, which are attributable to uncertainty of the surface CO_2 flux data. The models consistently underestimated the north-tropics mean gradient of CO_2 both in the free-troposphere and marine boundary layer during boreal summer. This result suggests that the north-tropics contrast of annual mean net non-fossil CO_2 flux should be greater than 2.7 Pg C yr^{-1} for 2007.

1 Introduction

Better understanding of the global and regional carbon budget would support more reliable prediction of future climate with an earth system model. However, the accuracy of source/sink estimation of carbon dioxide (CO_2) by inverse modeling, which is a leading method to estimate regional carbon budget, is not sufficiently high because of the errors in forward model transport and sparse observation coverage. In fact, inverted CO_2

ACPD
11, 12805–12848, 2011

fluxes are affected strongly by transport model properties. The so-called rectifier effect (Denning et al., 1996) tends to produce stronger uptake in northern terrestrial areas, thereby compensating stronger sources in tropical terrestrial areas in inversions. The TransCom3 models showed a large rectifier effect, on average, and consequently estimated a strong northern terrestrial sink of 2.4 Pg C yr^{-1} and strong tropical terrestrial source of 1.8 Pg C yr^{-1} (Gurney et al., 2004). However, this strong source/sink contrast has not been fully validated because of insufficient observational data for the tropics and because of large model uncertainties.

Later, using measurements of CO_2 obtained using aircraft at 12 sites, Stephens et al. (2007) showed the utility of vertical profiles in evaluating transport models and also inferred regional carbon budgets by selecting 3 out of 12 TransCom3 forward transport models. Investigating vertical CO_2 gradients, they suggested a smaller contrast of terrestrial flux between northern and tropical areas (1.6 Pg C yr^{-1}). However, the quality of the vertical CO_2 transport by model is insufficiently verified. Stephens et al. (2007) also suggested that most of the transport models were biased to ventilate too much of CO_2 uptake signal from the planetary boundary layer (PBL) to the free troposphere (FT) during boreal summer. Meanwhile, Yang et al. (2007) identified deficiencies in the vertical transport of the TransCom3 models by investigating vertical changes of seasonal amplitudes.

Moreover, our understanding of global-scale CO_2 distributions in FT remained limited. The aircraft measurement sites used in the previous studies were located mainly in mid-latitude to high latitude areas in the Northern Hemisphere. Especially, aircraft measurement networks have not fully covered the Asian areas such as South and Southeast Asia. Meanwhile, regional features of upper-air CO_2 have been surveyed over Europe and North America through aircraft campaigns (Gerbig et al., 2003; Sarrat et al., 2007; Crevoisier et al., 2010; Xueref-Remy et al., 2010).

In this study, we analyzed CO_2 model simulation results extensively using vertical profiles of CO_2, which are located throughout the globe, and surface measurements. The vertical profile measurements were taken from an aircraft CO_2 measurement

ACPD
11, 12805–12848, 2011

project: Comprehensive Observation Network for Trace gases by Airliner (CONTRAIL) (Machida et al., 2008; Matsueda et al., 2008; Sawa et al., 2008). The surface measurements were taken from GLOBALVIEW-CO_2 (2010). The CONTRAIL project measures atmospheric CO_2 concentrations covering altitudes between the earth's surface to the upper-troposphere/lower-stratosphere (UT/LS), and covering latitudes between the boreal high latitudes to the austral mid-latitudes including many parts of Asia. Although the vertical profiles from CONTRAIL are being used for validating inverse modelled fluxes (e.g., Chevallier et al., 2010), a detailed vertical profile comparison covering different ecophysical regions has not been conducted.

Therefore, the first aim of our study is to elucidate detailed structures of the atmospheric CO_2 in a three-dimensional view and to investigate model performances in reproducing those variations. The second aim is to draw some inferences to improve the precision of regional carbon budgets using the CONTRAIL measurements; such wide-ranging aircraft data have never been used in inversion studies before. Because the multi-model framework provides more robust results and improves the inference of the range of model uncertainty (Geels et al., 2007; Law et al., 2008; Patra et al., 2008), we used four independent forward transport models that were developed or updated recently. Furthermore, we used two datasets of surface CO_2 flux to evaluate the relative contributions of flux uncertainty to three-dimensional CO_2 concentration fields. We first describe the flux datasets, the transport models, and the observations as well as the simulation settings in Sect. 2. In the subsequent Sect. 3, we first introduce transport features of each model using simulation results of sulfur hexafluoride (SF_6) and radon (^{222}Rn). Subsequently, we show vertical profiles, seasonal variations and latitudinal profiles of the simulated and observed CO_2. Concluding remarks are presented in Sect. 4.

ACPD
11, 12805–12848, 2011

2 Experimental settings

The transport models were run using analyzed meteorology and prescribed surface fluxes during 2001–2007. The first five years (2001–2005) of the simulation were used as the model spin-up; the later period (2006–2007) was used for analysis in comparison with surface and aircraft observations. In addition to the CO_2 simulations, we simulated SF_6 and radon to investigate the overall model transport properties. All the initial concentrations were set to zero/constant everywhere.

2.1 Surface fluxes

The first set of CO_2 flux (Flux1) is bottom-up flux, prepared by combining seasonally varying fluxes of terrestrial biosphere photosynthesis/respiration from the Carnegie–Ames–Stanford Approach (CASA) model (Randerson et al., 1997), and of oceanic exchange based on CO_2 partial pressure measurements by oceanographic research vessels (Takahashi et al., 2009), and fossil fuel emissions with annual trends are further added. Fossil fuel emissions are derived from EDGAR-1998 distribution (Olivier and Berdowski, 2001) and the emission totals are scaled using the growth rate of top 20 country-specific fossil fuel consumptions from CDIAC (Boden et al., 2009). To consider a diurnal cycle of CO_2 flux from terrestrial ecosystems, the monthly means of CASA flux are distributed onto three-hourly time steps using 2 m air temperature and downward shortwave radiation data of Japanese 25-year ReAnalysis/JMA Climate Data Assimlation System (JRA-25/JCDAS) (Onogi et al., 2007) using the method described by Olsen and Randerson (2004). This experimental protocol resembles that of the TransCom continuous experiment (Law et al., 2008), except that we use interannually varying fossil CO_2 flux.

The second set (Flux2) is top-down/inversion flux combined with identical fossil fuel emissions as in Flux1. The inversion flux represents all non-fossil source/sink distribution over land and ocean, derived by inverse modeling with 12 TransCom3 models (Gurney et al., 2004) and observational data from GLOBALVIEW-CO_2 at 87 sites

ACPD
11, 12805–12848, 2011

during 1999–2001 (ref. Miyazaki et al. (2008) for an overall description). Although the period of 1999–2001 differs from this analysis period of 2006–2007, both periods commonly experienced La Niña (Southern Oscillation Indices are, respectively, *0.82*, *0.73*, 0.08 for 1999, 2000 and 2001, and −0.12, *0.24* for 2006 and 2007). Flux2 has large sink/source contrast between northern and tropical terrestrial areas (Table 1), similar to the previously described TransCom3 fluxes (Gurney et al., 2004; Baker et al., 2006).

The global total net fluxes for 2007 are, respectively, 7.0 Pg C yr^{-1} and 5.6 Pg C yr^{-1}, corresponding to Flux1 and Flux2. The non-fossil fuel fluxes of Flux1 and Flux2 are used repeatedly for different years.

The SF_6 emission distribution is taken from the EDGAR-1998 with the yearly emission change scaled to the global SF_6 growth rate estimated from measurements by Earth System Research Laboratory/National Oceanic and Atmospheric Administration (ESRL/NOAA). Radon emission data are referred from Jacob et al. (1997).

2.2 Transport models

We used three on-line models and one off-line model for the simulations. An on-line model calculates tracer transport within an atmospheric general circulation model (AGCM), in which meteorological fields are fully calculated and are nudged towards the analyzed fields using Newtonian relaxation methods (nudging). Meanwhile, in an off-line model, only tracer transport is calculated using already prepared meteorological fields from the analyzed data.

2.2.1 ACTM

The on-line chemical transport model ACTM is based on the Center for Climate System Research/National Institute for Environmental Studies/Frontier Research Center for Global Change (CCSR/NIES/FRCGC) AGCM. Cumulus convections are parameterized by the scheme of Arakawa and Schubert (1974). For vertical turbulent mixing, level 2 scheme of Mellor and Yamada (1974) is used. In the ACTM simulations, the

ACPD
11, 12805–12848, 2011

horizontal resolution of T42 spectral truncations (approximately 2.8° × 2.8°) is used. The number of the vertical layers is 32. For nudging, the ACTM uses six-hourly horizontal velocities and temperature from the National Center for Environmental Prediction/DOE AMIP-II Reanalysis (NCEP2; Kanamitsu et al., 2002). Further information of ACTM is available in Takigawa et al. (2005) and Patra et al. (2009).

2.2.2 MJ98-CDTM

The on-line model MJ98-CDTM was developed at the Japan Meteorological Agency (JMA) and the Meteorological Research Institute (MRI) (Shibata et al., 1999; Maki et al., 2009). The horizontal resolution of MJ98-CDTM is also T42; the number of vertical layers is 30. The vertical turbulent scheme is level 2 of Mellor and Yamada (1974). The Kuo (1974) scheme is used for deep cumulus convection and Tiedtke (1989) is used for shallow convection. The model uses the six-hourly horizontal wind velocities from JRA-25/JCDAS for nudging.

2.2.3 NICAM-TM

The Nonhydrostatic ICosahedral Atmospheric Model (NICAM; Tomita and Satoh, 2004; Satoh et al., 2008)-based transport model (NICAM-TM) was developed by Niwa (2010). The NICAM is a quasi-homogeneous grid AGCM: the horizontal grids are generated by dividing an icosahedron recursively. The tracer advection scheme preserves both monotonicity and consistency with continuity using a monotonic scheme of Miura (2007) (Niwa et al., 2011). The vertical turbulent scheme is MYNN Level 2 (Mellor and Yamada, 1974; Nakanishi and Niino, 2004; Noda et al., 2009). Cumulus convections are parameterized using the scheme of Arakawa and Schubert (1974). The NICAM simulations were performed using horizontal resolution of glevel-5 (5 is the number of divisions of an icosahedron to construct the horizontal grid; the grid interval is about 240 km). The number of vertical layers is 40 and the top of the model domain is about 45 km. The six-hourly horizontal wind velocities from JRA-25/JCDAS are used for nudging.

ACPD
11, 12805–12848, 2011

2.2.4 NIES

The National Institute for Environmental Studies (NIES) global transport model, with its flux-form advection algorithm (Belikov et al., 2011), is implemented on hybrid isentropic (σ-θ) vertical coordinate systems (model version denoted as NIES-08.1i.). The model is off-line and driven by JRA-25/JCDAS. Kuo-type penetrative cloud convection scheme is based on Grell (1993) including entrainment and detrainment processes on convective updrafts and downdrafts, as proposed by Tiedtke (1989). Cumulus convective updraft rate are calculated using the convective precipitation rate by JCDAS reanalysis, contrary to using large-scale moisture divergence used in Tiedtke (1989). The spatial resolution was set to 2.5° × 2.5° in the horizontal direction. The vertical coordinate contains 32 levels, with the isentropic part starting at 350 K. The three-hourly PBL height is taken from the ECMWF Interim Reanalysis (Simmons et al., 2007).

2.3 Aircraft and surface station measurements of CO_2

In the CONTRAIL project, measurement instruments are installed in commercial airliners. We used high-frequency data on Japan Airlines (JAL) flight paths obtained by five on-board continuous CO_2 measuring equipments (CMEs; Machida et al., 2008) during 2006–2007. From comparison with occasional flask sampling using automatic sampling equipment (ASE), the accuracy of the data is assured within 0.2 ppm (Matsueda et al., 2008). During 2006–2007, CONTRAIL measurement flights were conducted over East Asia (EAS), Europe (EUR), western North America (WNA), Hawaii (HWI), the Indian subcontinent (IND), northern and southern Southeast Asia (NSA, SSA), southern North America (SNA) and Australia (AUS) (Fig. 1 and Table 2). The measurement data were averaged for 1 min, corresponding to about 10–15 km horizontal distance at cruising altitude and 10 s corresponding to about 50–200 m vertical distance during ascent or descent near the airports. The measurement locations were corrected in advance according to the measurement lag time. The horizontal travelling length during taking-off and landing ranges about 200–400 km.

ACPD
11, 12805–12848, 2011

Surface CO_2 time series are taken from GLOBALVIEW-CO_2, a data product prepared using measurements from multiple institutions, following the methodology of Masarie and Tans (1995). To ascertain background features of surface CO_2, we chose 10 sites in marine boundary layer (MBL) from the dataset. The locations of those sites are portrayed in Fig. 1 and are also presented in Table 3.

2.4 Data processing for CO_2

The simulated atmospheric CO_2 data for 2006–2007 were extracted at the same time and locations as those of the CONTRAIL measurements by linear interpolation to the measurement space–time coordinates. In CONTRAIL measurements, altitude data are recorded as the pressure altitude. The model data were interpolated vertically using pressure data.

For the analysis, we used the detrended seasonal cycle of CO_2 (ΔCO_2) with reference to a linear trend at a background site because the simulated CO_2 growth rate is not optimized for the observed growth rate for 2006–2007. The simulated and observed data were, respectively subtracted using a linear trend function derived from each CO_2 record at Minamitorishima (24.30° N, 153.97° E), which is a remote marine site in the western North Pacific. First, the CO_2 record at Minamitorishima was fitted with a function combining linear trend with harmonics as

$$CO_2(t) = a_0 + a_1 t + \sum_{n=1}^{2} [a_{2n}\sin(2n\pi t) + a_{2n+1}\cos(2n\pi t)], \quad (1)$$

where t is time (calendar year) and a_i ($i = 0, 1, \ldots 5$) is a parameter optimized using least-squares method. Then the ΔCO_2 value at an arbitrary place x and time t was calculated as

$$\Delta CO_2(x,t) = CO_2(x,t) - a_0 - a_1 t. \quad (2)$$

Furthermore, the ΔCO_2 data were averaged into bins before analysis to avoid excessive weights of specific regions where measurements are conducted frequently (e.g.,

ACPD
11, 12805–12848, 2011

Japan). Bins are defined horizontally in each 10° × 10° latitude–longitude grid, vertically at each level with 1 km height, and temporally for each month.

3 Results and discussion

3.1 General features of the transport models

Figure 2 shows the latitudinal gradient of annual zonal mean of SF_6 concentrations at 400 hPa and 850 hPa. At both levels, MJ98-CDTM has the smallest north–south gradient (0.11, 0.21 ppt for 400 hPa and 850 hPa), whereas NIES has the largest one (0.18, 0.26 ppt for 400 hPa and 850 hPa). Because the emissions of SF_6 occur over more densely populated areas in the Northern Hemisphere than in the Southern Hemisphere, a smaller SF_6 gradient between the Northern and Southern Hemispheres indicates a faster inter-hemispheric exchange rate. Therefore, from Fig. 2, we infer that MJ98-CDTM has the fastest inter-hemispheric exchange rate and NIES has the slowest one. Within the range of the former two, the exchange rate of ACTM is on the slower side and that of NICAM-TM is on the faster side.

Figure 3 shows the horizontal distribution of the simulated radon concentrations at 300 hPa and 500 hPa for June–July–August (JJA). Results showed that MJ98-CDTM simulates much lower radon concentrations than the other three models (global averages of the radon mole fractions are 5.02, 1.84, 4.09, and 4.84×10^{-21}, respectively for ACTM, MJ98-CDTM, NICAM-TM, and NIES). Radon is a short-lived tracer. Therefore, the low radon concentration suggests that vertical transport of MJ98-CDTM is slower than those of the other models. At 500 hPa, however, the simulated radon concentrations are rather comparable with each other, although the ranking of the global average is the same as that at 300 hPa. The global averages of the radon mole fraction at 500 hPa are in the smaller range of $3.23–4.36 \times 10^{-21}$. Consequently, compared to the mid-troposphere, the radon concentration in the upper troposphere is quite sensitive to vertical transport, which is likely to be predominated by deep cumulus convection.

ACPD
11, 12805–12848, 2011

Those radon distribution patterns generally resemble those described in previous reports (Mahowald et al., 1997; Jacob et al., 1997; Dentener et al., 1999). Compared to those studies, the amounts of radon concentration in the upper troposphere (Fig. 3a) simulated by ACTM, NICAM-TM, and NIES are somewhat on the larger side and those by MJ98-CDTM are on the smaller side.

Figure 4 shows seasonal mean vertical differences of simulated atmospheric CO_2 between 850 hPa and 500 hPa for January–February–March (JFM) and July–August–September (JAS). For JFM, MJ98-CDTM simulated smaller differences over northern lands than the other models did. For JAS, both MJ98-CDTM and NIES simulated larger CO_2 vertical differences over northern land, although ACTM and NICAM-TM simulated smaller ones. Consequently, both ACTM and NICAM-TM have weaker vertical mixing between 850 hPa and 500 hPa for boreal winter and stronger one for boreal summer. In contrast, MJ98-CDTM has a stronger one for boreal winter and a weaker one for boreal summer. In the case of NIES, it is on the weaker side for both boreal winter and summer.

3.2 Vertical profiles over the airports

Figure 5 presents seasonally varying vertical profiles of the CONTRAIL CO_2 measurements and the model simulations over each area, the spatial coverage of which is presented in Fig. 1. As the figure shows, the models reasonably reproduced the observed vertical profiles; averaged correlation coefficients of each vertical profile between the observation and the model mean are 0.63 and 0.71, respectively, for the results obtained using Flux1 and Flux2. In addition, the result suggests that vertical profiles have measurable sensitivity to surface flux. Moreover, because the CONTRAIL measurements were not used in the inversion of Flux2, i.e. independent data, the improvement of the correlation by Flux2 shows some validity of the inversion.

ACPD
11, 12805–12848, 2011

3.2.1 Northern areas (EAS, EUR, WNA, HWI)

Over northern areas on the edge of landmass (EAS, EUR, WNA), large vertical gradients up to about 4 ppm are observed between near surface and FT. Then they seasonally vary in a wide range (Fig. 5a–c). Furthermore, during boreal winter–spring (JFM and AMJ), the CONTRAIL measurements show large vertical gradients (ca. 4 ppm) in the UT/LS region. Meanwhile, in HWI, much smaller gradients (ca. 2 ppm) are observed from near the surface to the upper troposphere throughout the year (Fig. 5d). Those vertical profile patterns are almost reproduced by the models (the averaged correlation coefficients are 0.80 and 0.87, respectively, for Flux1 and Flux2).

During boreal summer, differences between Flux1 and Flux2 are considerably large in northern terrestrial areas (during JAS, Flux2 has 1.9 $\mathrm{Pg\,C\,yr^{-1}}$ larger uptake than Flux1). This flux difference caused significant changes of the vertical profiles for JAS. Especially in EUR and WNA, Flux2 consistently improved the model–observation agreement. Root mean square differences (RMSD) are lower by 0.4 and 0.2 ppm, respectively, for EUR and WNA.

However, most simulated vertical gradients from PBL to FT are still smaller than the observed ones during boreal summer, except EAS. One probable cause is a deficiency of the model vertical transport. Actually, Stephens et al. (2007) reported that the TransCom3 models have overly strong vertical mixing from PBL to FT during boreal summer. For this study, however, we cannot completely attribute the model–observation discrepancy to the model deficiency. We consider that flux uncertainty is significant to the simulated PBL-FT gradients because the PBL-FT gradients were changed greatly by selection of the surface flux for JAS.

3.2.2 Indian subcontinent (IND)

Over the Indian subcontinent (IND), model–observation mismatches of the vertical profiles are larger than those of the northern profiles (the averaged RMSD by Flux2 is 1.28 ppm for all seasons) (Fig. 5e). Especially, in JAS, the models overestimated

ACPD
11, 12805–12848, 2011

ΔCO_2 at all levels and failed to reproduce the large vertical gradient near the surface (the averaged RMSD by Fux2 is 2.41 ppm). This fact suggests the need to put stronger sinks in that area of the flux data. Vigorous vertical transport within the Indian summer monsoon circulation rapidly ventilated low CO_2 air from near the surface to the upper troposphere, which the models were unable to reproduce because of insufficient sinks. It engenders a noticeable model–observation mismatch in FT. Actually, we confirmed a strong impact of surface flux on the simulated vertical profiles. The models with Flux1, which has a 12.4 g C m^{-2} stronger net sink than Flux2 in IND for JAS, simulated the vertical profiles closer to the observed one (the averaged RMSD = 1.69 ppm), although it is still insufficient. The large model–observation mismatch is attributable to the fact that flux inhomogeneity in the Indian region is not constrained in Flux2 because the inversion of Flux2 had a large flux estimate region there that includes East Asia, South Asia, and Central Asia. A more detailed inversion study by Patra et al. (2011) estimated a large CO_2 uptake of about 1.8 Pg C yr^{-1} during the summer in South Asia using ACTM as a forward transport model, GLOBALVIEW-CO_2 data product and flask measurements of CARIBIC (Schuck et al., 2010), and was subsequently validated by comparison with CONTRAIL data over Delhi and in the upper troposphere. Here, we used four different models to confirm the requirement of the strong sink.

Results also show pronounced model–observation mismatches (RMSD by Flux2 is 1.11 ppm) for AMJ. The CONTRAIL measurement shows high CO_2 near the surface and a consequently large PBL-FT gradient. However the models failed to reproduce it. Those mismatches are especially prominent in April (not shown). Over the Indian subcontinent, the period of April corresponds to the end of the dry season. The air temperature is quite high during the period. Therefore, that model underestimation might result from further sources from terrestrial biosphere respirations or biomass burnings (Patra et al., 2011).

ACPD
11, 12805–12848, 2011

3.2.3 Southeast Asia (NSA, SSA)

Features of the vertical profile over Southeast Asia differ greatly from those in northern areas (Fig. 5f,g). Both over NSA and SSA, CO_2 concentrations in the upper troposphere are about 1–2 ppm higher than those near the surface for AMJ. During this season, net non-fossil CO_2 flux in Southeast Asia and western Pacific is not a strong sink but a rather weak source (0.50, 0.77 Pg C yr^{-1}, respectively for Flux1 and Flux2). Therefore, the feature of CO_2 concentration increasing with height is probably induced by surface CO_2 signals from other areas that were transported through the upper troposphere. The models more or less captured that feature.

Over NSA, a large PBL-FT gradient (ca. 4 ppm) was observed during JFM, but the models consistently failed to reproduce it. Indochina experiences dry atmospheric conditions during those months. Therefore, model–observation mismatches might result from strong sources from biosphere respirations or biomass burnings that are not represented in the flux data.

Over SSA, the average ΔCO_2 simulated from Flux2 is 0.7 ppm larger throughout a year and 0.37 ppm closer to the observed one than that from Flux1. The Flux1–Flux2 difference of the annual net flux in Southeast Asia and western Pacific is small (0.06, −0.04 Pg C yr^{-1}, respectively for Flux1 and Flux2). Therefore, the improvement of the model–observation mismatch by Flux2 is attributed to other large-scale flux patterns. Probably, it is induced by strong annual net sources in other terrestrial tropical areas of Flux2 (see Table 1).

It should also be noted that all the models marginally failed to reproduce steep vertical gradients of 1–2 ppm near the surface over SSA persisting in all seasons. This failure is mostly attributable to the representation error of fossil-fuel emission. Probably, a large amount of fossil fuel emissions on a small island, such as Jakarta on Java Island, is not well represented in the model grids. A test simulation by ACTM using recently updated fossil fuel emission data (EDGAR-4, 2009), in which a strong source marginally exists on Java Island, we produced a closer vertical gradient to the observed one (not shown).

ACPD
11, 12805–12848, 2011

3.2.4 Southern North America (SNA)

Over SNA, results show apparent model–observation mismatches of vertical gradients at lower altitudes, which are much larger than the model–model differences (Fig. 5h). In the area, JAL airplanes arrive and depart at the airport in Mexico City, which is located in a basin surrounded by high mountains. This topography strongly traps polluted air near the surface. However, in the global models, the topography is smoothed out and such phenomena are not well represented in the global models.

3.2.5 Australia (AUS)

Over AUS, atmospheric CO_2 largely varies not only at lower altitudes but also in the UT/LS region (Fig. 5i). The feature of high CO_2 in the upper troposphere during AMJ is similar to those over Southeast Asia, which suggests that high-CO_2 air from the Northern Hemisphere intruded into the Southern Hemisphere through the tropical upper troposphere. This transport mechanism has already been indicated from air sampling measurements of commercial airlines between Japan and Australia conducted by Nakazawa et al. (1991) and Matsueda et al. (2002), which are a predecessor and a part of the current CONTRAIL project. Furthermore, the theoretical framework of the inter-hemispheric transport of CO_2 is explained by Miyazaki et al. (2008) using ACTM simulation. For this study, we confirmed that mechanism from the vertical profiles. For AMJ, the models show the same increasing profiles as the observed one, but model–model differences are quite large. Those differences are induced by differences of the inter-hemispheric exchange rate among the models. For all the seasons, the highest mean ΔCO_2 is simulated by MJ98-CDTM, which has the fastest inter-hemispheric exchange, whereas the lowest mean ΔCO_2 is simulated by NIES, which has the slowest one (Fig. 2).

ACPD
11, 12805–12848, 2011

3.3 Seasonal variations

Figure 6 portrays seasonal mean variations of the simulated and observed CO_2 at 5–6 km over each area using data for 2006–2007. Each seasonal variation is derived from the binned ΔCO_2 data. Over most areas, seasonal amplitudes simulated from Flux2 are larger and closer to the observed one than those from Flux1 (Table 4). Furthermore, Flux2 improves correlations of seasonal variations between the observation and the simulations (Table 4), supporting the fact that Flux2 is more favourable to simulate CO_2 for this period. However, the seasonal amplitudes simulated from Flux2 are still smaller than the observed one over all the areas.

3.3.1 North

For comparison of CO_2 seasonal variations from at surface background sites in MBL to the upper troposphere, we averaged seasonal variations of the simulated and observed CO_2 at 4–5 km and 7–8 km in FT and in MBL of the northern area (Fig. 7). CONTRAIL has fewer measurement gaps during 2007 (see each upper panel in Fig. 5). Therefore, we used only data for 2007 here. The seasonal variation in FT is derived by averaging seasonal variations over three northern areas (EAS, EUR, and WNA). For MBL, we averaged seasonal variations from CO_2 records at 6 MBL sites located between 20° N and 70° N, which are also detrended by the linear trend at Minamitorishima.

Using northern CO_2 vertical profiles, Yang et al. (2007) calculated amplitude ratios of seasonal variations at upper and lower levels, and suggested that the TransCom3 models underestimated vertical propagation speed of seasonal variation in FT. We calculated similar amplitude ratios using the amplitude at 4–5 km as the reference. The seasonal amplitude ratios at 7–8 km simulated by ACTM, NICAM-TM, and NIES (0.81–0.89) are comparable to the observed one (0.86), irrespective of flux data used (Table 5). It indicates that those models reasonably simulated the vertical propagation of seasonal CO_2 variation within FT, differently from the TransCom3 models. Compared to those models, MJ98-CDTM shows quite a small amplitude ratio (0.69, 0.73 for Flux1,

ACPD
11, 12805–12848, 2011

Flux2). This underestimation by MJ98-CDTM is related to the slower vertical transport inferred from the lower radon concentration in the upper troposphere compared to the other three models (Fig. 3a).

Meanwhile, the model–model difference of amplitude ratio in MBL are rather large (1.26–1.69), indicating large model uncertainty for vertical transport from the near surface to FT. Furthermore, flux uncertainty should also be noted, as indicated by significant changes of the amplitude ratio by the fluxes (15–30%). These ratio changes according to the fluxes also indicate that the CONTRAIL measurements in FT caught different signals of surface CO_2 flux from those caught by the MBL sites. Probably, that is true because CONTRAIL measurements are affected by terrestrial fluxes more strongly than the MBL ones are, justifiably because of their continental locations. In contrast, the amplitude ratios at 7–8 km are not so affected by the fluxes. This small impact of the fluxes indicates that seasonal flux signals are almost identical at 4–5 km and 7–8 km.

3.3.2 Tropics

Figure 8 shows the same seasonal variations as those shown in Fig. 7, but for two tropical areas. The seasonal variations in FT are derived, respectively from the binned ΔCO_2 data over the Southeast areas of NSA and SSA. The MBL seasonal variations are derived, respectively from CO_2 records at Guam and Christmas Island, which are located latitudinally near each Southeast Asian area.

Over NSA, the seasonal amplitude at 4–5 km is about 1 ppm smaller than that at each MBL site, although the seasonal amplitude at 7–8 km is larger (Fig. 8). Seasonal amplitudes in FT over SSA are a half to a third of those over NSA; furthermore, they have two minima, whereas the MBL one has one minimum. The models simulated most of those features (the correlations are more than 0.7). However, the models consistently underestimated seasonal amplitudes, as they do in the northern area. Especially, the model–observation mismatches at the seasonal maximum and minimum are notable at 7–8 km, which also suggests the intrusion of CO_2, as discussed in Sect. 3.2; the

ACPD
11, 12805–12848, 2011

seasonal CO_2 variation in the Northern Hemisphere intruded towards the south via the tropical upper troposphere. Consequently the models underestimated the seasonal amplitude over tropics.

3.4 Latitudinal profiles

Figure 9 shows the latitudinal mean profile of ΔCO_2 at 5–6 km in FT and in MBL for JFM and JAS of 2007. During JFM, both at 5–6 km and in MBL, the observed latitudinal profile is in the range of the model uncertainty. At 5–6 km, the simulated profile is apparently affected by the inter-hemispheric exchange rate; MJ98-CDTM, which has the fastest inter-hemispheric exchange rate, showed the smallest simulated inter-hemispheric gradient (2.3 ppm), whereas NIES, which has the slowest inter-hemispheric exchange rate, showed the largest simulated inter-hemispheric gradient (3.4 ppm). Meanwhile, in MBL, the simulated profiles are in a much wider range (2.4–4.3 ppm). Probably the simulated profile is affected not only by inter-hemispheric exchange but also by vertical mixing near the surface. This model–model difference is apparently greater than differences by the fluxes, indicating that the model uncertainty is predominant to the latitudinal profile in MBL during boreal winter.

In contrast, during JAS, the results are quite sensitive to the flux data. At 5–6 km, the north-tropics mean gradients (north: 20–70° N, tropics: 20° S–20° N) simulated from Flux2 are 0.5–0.8 ppm larger than those from Flux1 (Table 6a) and those differences are comparable to or greater than model–model differences, which suggests that active summer vertical transport ventilates some significant flux signals up to FT. However, we found apparent discrepancies between the observed and simulated north-tropics mean gradients. At 5–6 km and in MBL, the gradients of 5.2 and 1.8 ppm are observed, respectively. All the models with Flux2 underestimated those by 0.3–2.0 and 0.5–1.1 ppm (mean CO_2 in tropics is larger than that in north).

Actually, the north-tropics CO_2 gradient should reflect the flux contrast between the two areas. Therefore, the smaller simulated north-tropics gradient indicates requirements of stronger net carbon sink in the northern area and/or stronger net source

ACPD
11, 12805–12848, 2011

in the tropics in the flux data. It is noteworthy that this discussion is not affected strongly by model uncertainty for vertical transport because the model underestimation of the north-tropics mean gradient is consistent both in FT and MBL. Here, we infer the stronger terrestrial net sink in the northern area during boreal summer. At the MBL sites for 2007, the observed growth rate is 0.8 ppm yr^{-1} smaller than the simulated one from Flux2, on average. That discrepancy is 0.5 ppm yr^{-1} larger in the northern area than that in the tropical area. These facts indicate further sinks in the northern area during boreal summer. Moreover, compared to that in MBL, the models largely underestimated the north-tropics mean gradient observed by CONTRAIL in FT. Using Flux2, the degrees of the model underestimation of the north-tropics mean gradient in FT are 10–44% larger than those in MBL. The CONTRAIL data in FT are more likely to be affected by terrestrial fluxes, as discussed in the previous section. Therefore, it is suggested that most of the further sinks should exist in northern terrestrial areas. One prominent candidate of those sinks is the strong uptake in IND (20–30° N) that was inferred from the vertical profile comparison (Sect. 3.2.2). The possibility of a stronger net source in the tropics during boreal summer is ruled out because the tropics-south mean gradient of CO_2 is well simulated by the models.

The annual mean of the observed north-tropics gradients at 5–6 km and in MBL are, respectively, 0.6 and 0.8 ppm (Table 6). The models mostly overestimated gradients by about 0.1–0.5 ppm at 5–6 km and by about 0.2 ppm in MBL using Flux2. This is predominantly contributed by the large model–observation mismatch of the JAS gradients. The result suggests that the north-tropics contrast of annual mean net surface CO_2 flux should be larger than that of Flux2, which has non-fossil carbon budgets of -1.38 Pg C yr^{-1} and 1.35 Pg C yr^{-1}, respectively for northern and tropical terrestrial areas (Table 1). Therefore, the north-tropics contrast of annual mean net non-fossil CO_2 flux is inferred to be larger than 2.7 Pg C yr^{-1}. It indicates that if we use non-fossil CO_2 flux which has the annual north-tropics contrast of 1.6 Pg C yr^{-1} as suggested by Stephens et al. (2007), we might be unable to reproduce the observed north-tropics mean gradient of CO_2 for 2007.

ACPD
11, 12805–12848, 2011

4 Conclusions

We elucidated three-dimensional structures of atmospheric CO_2 extensively using globally located vertical profile measurements of CONTRAIL and surface measurements of GLOBALVIEW. We investigated model performances in reproducing the three-dimensional CO_2 structures and their variations. Furthermore, using four independent transport models and two different fluxes, we evaluated the relative contributions of model and flux uncertainties. Furthermore, new implications for regional carbon budgets were obtained by comparing the simulations and the observations.

In general, the models reproduced the spatiotemporal patterns of CO_2 concentrations observed by CONTRAIL. Seasonal mean vertical profiles and vertical propagation of seasonal variation in the FT are mostly well simulated by the models. Furthermore, we confirmed reasonable model performance for reproducing CO_2 variations even over Southeast Asia, where measurements have not been conducted sufficiently to date. The CONTRAIL measurements suggested that northern CO_2 intruded southward through the upper troposphere. We confirmed that the models simulated that feature overall. In terms of the correlation coefficient, root-mean-square difference, and seasonal amplitude, the CO_2 concentration field simulated from Flux2 is closer to the observed one than that from Flux1, indicating some validity of the inversion that produced Flux2.

However, results show marked discrepancies between the observations and simulations. Especially, the discrepancy over the Indian continent during July–August–September is noteworthy; it indicates quite a strong carbon sink in that area, which has been unconstrained by the prior inversion. Another notable model–observation discrepancy was found in the PBL-FT gradient over northern Southeast Asia for January–February–March, which indicates strong sources from biosphere respiration or biomass burnings induced by dry atmosphere condition. From comparison of latitudinal profiles in FT and MBL, we infer a strong terrestrial net sink in the northern area during the boreal summer of 2007. The overestimation of annual mean of the

ACPD
11, 12805–12848, 2011

north-tropics gradient indicates large north-tropics contrast of net non-fossil CO_2 flux for 2007 as greater than 2.7 Pg C yr^{-1}.

Acknowledgements. We are grateful to the many engineers of Japan Airlines, JAMCO Tokyo for operating the measurement system. We would like to acknowledge JAL Foundation for coordinating the CONTRAIL project. The CONTRAIL project is financially supported by the Research Fund by Global Environmental Research Coordination System of the Ministry of the Environment (MOE) in Japan. Our appreciation is also extended to the many research groups contributing to the GLOBALVIEW-CO_2 data product. The datasets used for this study were provided by the cooperative research project of the JRA-25/JCDAS long-term reanalysis by Japan Meteorological Agency (JMA) and Central Research Institute of Electric Power Industry (CRIEPI). YN thanks Hirofumi Tomita and other members at Research Institute for Global Change/JAMSTEC and at The University of Tokyo for developing NICAM.

References

Arakawa, A. and Schubert, W.: Introduction of cumulus cloud ensemble with the large-scale environment. Part I, J. Atmos. Sci., 31, 671–701, 1974.

Baker, D. F., Law, R. M., Gurney, K. R., Rayner, P., Peylin, P., Denning, A. S., Bousquet, P., Bruhwiler, L., Chen, Y.-H., Ciais, P., Fung, I. Y., Heimann, M., John, J., Maki, T., Maksyutov, S., Masarie, K., Prather, M., Pak, B., Taguchi, S., and Zhu, Z.: TransCom 3 inversion intercomparison: impact of transport model errors on the interannual variability of regional CO_2 fluxes, 1988–2003, Global Biogeochem. Cy., 20, GB1002, doi:10.1029/2004GB002439, 2006.

Belikov, D., Maksyutov, S., Miyasaka, T., Saeki, T., Zhuravlev, R., and Kiryushov, B.: Mass-conserving tracer transport modelling on a reduced latitude-longitude grid with NIES-TM, Geosci. Model Dev., 4, 207–222, doi:10.5194/gmd-4-207-2011, 2011.

Boden, T. A., Marland, G., and Andres, R. J.: Global, Regional, and National Fossil Fuel CO_2 Emissions, Carbon Dioxide Information Analysis Center, Oak Ridge National Laboratory, U.S. Department of Energy, Oak Ridge, Tenn, USA, doi:10.3334/CDIAC/00001 (last access: March 2010), 2009.

Chevallier, F., Ciais, P., Conway, T. J., Aalto, T., Anderson, B. E., Bousquet, P., Brunke, E. G., Ciattaglia, L., Esaki, Y., Fröhlich, M., Gomez, A., Gomez-Pelaez, A. J., Haszpra, L., Krum-

ACPD

11, 12805–12848, 2011

mel, P. B., Langenfelds, R. L., Leuenberger, M., Machida, T., Maignan, F., Matsueda, H., Morguí, J. A., Mukai, H., Nakazawa, T., Peylin, P., Ramonet, M., Rivier, L., Sawa, Y., Schmidt, M., Steele, L. P., Vay, S. A., Vermeulen, A. T., Wofsy, S., and Worthy, D.: CO_2 surface fluxes at grid point scale estimated from a global 21 year reanalysis of atmospheric measurements, J. Geophys. Res., 115, D21307, doi:10.1029/2010JD013887, 2010.

Crevoisier, C., Sweeney, C., Gloor, M., Sarmiento, J. L., and Tans, P. P.: Regional US carbon sinks from three-dimensional atmospheric CO_2 sampling, P. Natl. Acad. Sci USA, 107, 18348–18353, 2010.

Denning, A. S., Randall, D. A., Collatz, G. J., and Sellers, P. J.: Simulations of terrestrial carbon metabolism and atmospheric CO_2 in a general circulation model. Part 2: Spatial and temporal variations of atmospheric CO_2, Tellus, 48B, 543–567, 1996.

Dentener, F., Feichter, J., and Jeuken, A.: Simulation of the transport of Rn^{222} using on-line and off-line global models at different horizontal resolutions: a detailed comparison with measurements, Tellus, 51B, 573–602, 1999.

EDGAR-4: European Commission, Joint Research Centre (JRC)/Netherlands Environmental Assessment Agency (PBL), Emission Database for Global Atmospheric Research (EDGAR), release version 4.0, available at: http://edgar.jrc.ec.europa.eu (last access: November 2009), 2009.

Geels, C., Gloor, M., Ciais, P., Bousquet, P., Peylin, P., Vermeulen, A. T., Dargaville, R., Aalto, T., Brandt, J., Christensen, J. H., Frohn, L. M., Haszpra, L., Karstens, U., Rödenbeck, C., Ramonet, M., Carboni, G., and Santaguida, R.: Comparing atmospheric transport models for future regional inversions over Europe – Part 1: mapping the atmospheric CO_2 signals, Atmos. Chem. Phys., 7, 3461–3479, doi:10.5194/acp-7-3461-2007, 2007.

Gerbig, C., Lin, J. C., Wofsy, S. C., Daube, B. C., Andrews, A. E., Stephens, B. B., Bakwin, P. S., and Grainger, C. A.: Toward constraining regional-scale fluxes of CO_2 with atmospheric observations over a continent: 1. Observed spatial variability from airborne platforms, J. Geophys. Res., 108(D24), 4756, doi:10.1029/2002JD003018, 2003.

GLOBALVIEW-CO_2: Cooperative Atmospheric Data Integration Project–Carbon Dioxide CD-ROM, NOAA CMDL, Boulder, Colorado, available via anonymous FTP at: ftp.cmdl.noaa.gov, Path:ccg/co2/GLOBALVIEW, (last access: February 2010), 2010.

Grell, G. A.: Prognostic evaluation of assumptions used by cumulus parameterizations, Mon. Weather Rev., 121, 764–787, 1993.

Gurney, K. R., Law, R. M., Denning, A. S., Rayner, P. J., Pak, B. C., Baker, D., Bousquet, P.,

ACPD
11, 12805–12848, 2011

Bruhwiler, L., Chen, Y.-H., Ciais, P., Fung, I. Y., Heimann, M., John, J., Maki, T., Maksyutov, S., Peylin, P., Prather, M., and Taguchi, S.: Transcom 3 inversion intercomparison: model mean results for the estimation of seasonal carbon sources and sinks, Global Biogeochem. Cy., 18, GB1010, doi:10.1029/2003GB002111, 2004.

Jacob, D. J., Prather, M. J., Rasch, P. J., Shia, R.-L., Balkanski, Y. J., Beagley, S. R., Bergmann, D. J., Blackshear, W. T., Brown, M., Chiba, M., Chipperfield, M. P., Grandprè, J. D., Dignon, J. E., Feichter, J., Genthon, C., Grose, W. L., Kashibhatla, P. S., Köhler, I., Kritz, M. A., Law, K., Penner, J. E., Ramonet, M., Reeves, C. E., Rotman, D. A., Stockwell, D. Z., Velthoven, P. F. J. V., Verver, G., Wild, O., Yang, H., and Zimmermann, P.: Evaluation and intercomparison of global atmospheric transport models using ^{222}Rn and other short-lived tracers, J. Geophys. Res., 102, 5953–5970, 1997.

Kanamitsu, M., Ebisuzaki, W., Woolen, J., Potter, J., and Fiorino, M.: NCEP/DOE AMPI-II reanalysis (R-2), B. Am. Meteorl. Soc., 83, 1631–1643, 2002.

Kuo, H. L.: Fur ther studies of the parameterization of the influence of cumulus convection on large scale flow, J. Atmos. Sci., 31, 1232–1240, 1974.

Law, R. M., Peters, W., Rödenbeck, C., Aulagnier, C., Baker, I., Bergmann, D. J., Bousquet, P., Brandt, J., Bruhwiler, L., Cameron-Smith, P. J., Christensen, J. H., Delage, F., Denning, A. S., Fan, S., Geels, C., Houweling, S., Imasu, R., Karstens, U., Kawa, S. R., Kleist, J., Krol, M. C., Lin, S.-J., Lokupitiya, R., Maki, T., Maksyutov, S., Niwa, Y., Onishi, R., Parazoo, N., Patra, P. K., Pieterse, G., Rivier, L., Satoh, M., Serrar, S., Taguchi, S., Takigawa, M., Vautard, R., Vermeulen, A. T., and Zhu, Z.: TransCom model simulations of hourly atmospheric CO_2: experimental overview and diurnal cycle results for 2002, Global Biogeochem. Cy., 22, GB3009, doi:10.1029/2007GB003050, 2008.

Machida, T., Matsueda, H., Sawa, Y., Nakagawa, Y., Hirotani, K., Kondo, N., Goto, K., Nakazawa, T., Ishikawa, K., and Ogawa, T.: Worldwide measurements of atmospheric CO_2 and other trace gas species using commercial airlines, J. Atmos. Ocean. Tech., 25, 1744–1754, 2008.

Mahowald, N. M., Rasch, P. J., Eaton, B. E., Whittlestone, S., and Prinn, R. G.: Transport of ^{222}radon to the remote troposphere using the model of atmospheric transport and chemistry and assimilated winds from ECMWF and the National Center for Environmental Prediction/NCAR, J. Geophys. Res., 102, 28139–28151, 1997.

Maki, T., Ikegami, M., Fujita, T., Yamada, K., Sawa, Y., Matsueda, H., Shibata, K., Niwa, Y., Patra, P. K., and Machida, T.: Development of on-line tracer transport model and validation

ACPD
11, 12805–12848, 2011

of vertical tracer transport against aircraft data, 8th International Carbon Dioxide Conference, Jena, Germany, 13–19 September 2009, T4-014, 2009.
Masarie, K. A. and Tans, P. P.: Extension and integration of atmospheric carbon dioxide data into a globally consistent measurement record, J. Geophys. Res., 100, 11593–11610, 1995.
Matsueda, H., Inoue, H. Y., and Ishii, M.: Aircraft observation of carbon dioxide at 8–13 km altitude over the Western Pacific from 1993 to 1999, Tellus, 54B, 1–21, 2002.
Matsueda, H., Machida, T., Sawa, Y., Nakagawa, Y., Hirotani, K., Ikeda, H., Kondo, N., and Goto, K.: Evaluation of atmospheric CO_2 measurements from new flask air sampling of JAL airliner observations, Pap. Meteorol. Geophys., 59, 1–17, 2008.
Mellor, G. L. and Yamada, T.: A hierarchy of turbulence closure models for planetary boundary layers, J. Atmos. Sci., 31, 1791–1806, 1974.
Miura, H.: An upwind-biased conservative advection scheme for spherical hexagonal–pentagonal grids, Mon. Weather Rev., 135, 4038–4044, 2007.
Miyazaki, K., Patra, P. K., Takigawa, M., Iwasaki, T., and Nakazawa, T.: Global-scale transport of carbon dioxide in the troposphere, J. Geophys. Res., 113, D15301, doi:10.1029/2007JD009557, 2008.
Nakanishi, M. and Niino, H.: An improved Mellor–Yamada level 3 model with condensation physics: its design and verification, Bound.-Lay. Meteorol., 112, 1–31, 2004.
Nakazawa, T., Miyashita, K., Aoki, S., and Tanaka, M.: Temporal and spatial variations of upper tropospheric and lower stratospheric carbon dioxide, Tellus, 43B, 106–117, 1991.
Niwa, Y.: Numerical study on atmospheric transport and surface source/sink of carbon dioxide, Ph.D. thesis, Center for Climate System Research, The University of Tokyo, Japan, 178 pp., 2010.
Niwa, Y., Tomita, H., Satoh, M., and Imasu, R.: A three-dimensional icosahedral grid advection scheme preserving monotonicity and consistency with continuity for atmospheric tracer transport, J. Meteorol. Soc. Jpn., in press, 2011.
Noda, A. T., Oouchi, K., Satoh, M., Tomita, H., Iga, S.-I., and Tsushima, Y.: Importance of the subgrid-scale turbulent moist process of the turbulent transport: on cloud distribution in global cloud-resolving simulations, Atmos. Res., 96, 208–217, doi:10.1016/j.atmosres.2009.05.007, 2009.
Olivier, J. G. J. and Berdowski, J. J. M.: Global emissions sources and sinks, A.A. Balkema Publishers/Swets & Zeitlinger Publishers, Lisse, The Netherlands, 2001.
Olsen, S. C. and Randerson, J. T.: Differences between surface and column atmo-

ACPD
11, 12805–12848, 2011

spheric CO_2 and implications for carbon cycle research, J. Geophys. Res., 109, D02301, doi:10.1029/2003JD003968, 2004.
Onogi, K., Tsutsui, J., Koide, H., Sakamoto, M., Kobayashi, S., Hatsushika, H., Matsumoto, T., Yamazaki, N., Kamahori, H., Takahashi, K., Kadokura, S., Wada, K., Kato, K., Oyama, R., Ose, T., Mannoji, N., and Taira, R.: The JRA-25 reanalysis, J. Meteorol. Soc. Jpn., 85, 369–432, 2007.
Patra, P. K., Law, R. M., Peters, W., Rödenbeck, C., Takigawa, M., Aulagnier, C., Baker, I., Bergmann, D. J., Bousquet, P., Brandt, J., Bruhwiler, L., Cameron-Smith, P. J., Christensen, J. H., Delage, F., Denning, A. S., Fan, S., Geels, C., Houweling, S., Imasu, R., Karstens, U., Kawa, S. R., Kleist, J., Krol, M. C., Lin, S.-J., Lokupitiya, R., Maki, T., Maksyutov, S., Niwa, Y., Onishi, R., Parazoo, N., Pieterse, G., Rivier, L., Satoh, M., Serrar, S., Taguchi, S., Vautard, R., Vermeulen, A. T., and Zhu, Z.: TransCom model simulations of hourly atmospheric CO_2: analysis of synoptic-scale variations of the period 2002–2003, Global Biogeochem. Cy., 22, GB4013, doi:10.1029/2007GB003081, 2008.
Patra, P. K., Takigawa, M., Dutton, G. S., Uhse, K., Ishijima, K., Lintner, B. R., Miyazaki, K., and Elkins, J. W.: Transport mechanisms for synoptic, seasonal and interannual SF_6 variations and "age" of air in troposphere, Atmos. Chem. Phys., 9, 1209–1225, doi:10.5194/acp-9-1209-2009, 2009.
Patra, P. K., Niwa, Y., Schuck, T. J., Brenninkmeijer, C. A. M., Machida, T., Matsueda, H., and Sawa, Y.: Carbon balance of South Asia constrained by passenger aircraft CO_2 measurements, Atmos. Chem. Phys. Discuss., 11, 5379–5405, doi:10.5194/acpd-11-5379-2011, 2011.
Randerson, J. T., Thompson, M. V., Conway, T. J., Fung, I. Y., and Field, C. B.: The contribution of terrestrial sources and sinks to trends in the seasonal cycle of atmospheric carbon dioxide, Global Biogeochem. Cy., 11, 535–560, 1997.
Sarrat, C., Noihan, J., Lacarrére, P., Conier, S., Lac, C., Calvet, J. C., Dolman, A. J., Gerbig, C., Neininger, B., Ciais, P., Paris, J. D., Boumard, F., Ramonet, M., and Butet, A.: Atmospheric CO_2 modeling at the regional scale: application to the CarboEurope Regional Experiment, J. Geophys. Res., 112, D12105, doi:10.1029/2006JD008107, 2007.
Satoh, M., Matsuno, T., Tomita, H., Miura, H., Nasuno, T., and Iga, S.: Nonhydrostatic icosahedral atmospheric model (NICAM) for global cloud resolving simulations, J. Comput. Phys., 227, 3486–3514, 2008.
Sawa, Y., Machida, T., and Matsueda, H.: Seasonal variations of CO_2 near the tropopause ob-

ACPD
11, 12805–12848, 2011

served by commercial aircraft, J. Geophys. Res., 113, D23301, doi:10.1029/2008JD010568, 2008.
Schuck, T. J., Brenninkmeijer, C. A. M., Baker, A. K., Slemr, F., von Velthoven, P. F. J., and Zahn, A.: Greenhouse gas relationships in the Indian summer monsoon plume measured by the CARIBIC passenger aircraft, Atmos. Chem. Phys., 10, 3965–3984, doi:10.5194/acp-10-3965-2010, 2010.
Shibata, K., Yoshimura, H., Ohizumi, M., Hosaka, M., and Sugi, M.: A simulation of troposphere, stratosphere and mesosphere with an MRI/JMA98 GCM, Pap. Meteorol. Geophys., 50, 15–53, 1999.
Simmons, A., Uppala, S., Dee, D., and Kobayashi, S.: ERA-Interim: New ECMWF reanalysis products from 1989 onwards, ECMWF Newsl., 110, 25–35, 2007.
Stephens, B. B., Gurney, K. R., Tans, P. P., Sweeney, C., Peters, W., Bruhwiler, L., Ciais, P., Ramonet, M., Bousquet, P., Nakazawa, T., Aoki, S., Machida, T., Inoue, G., Vinnichenko, N., Lloyd, J., Jordan, A., Heimann, M., Shibistova, O., Langenfelds, R. L., Steele, L. P., Francey, R. J., and Denning, A. S.: Weak northern and strong tropical land carbon uptake from vertical profiles of atmospheric CO_2, Science, 316, 1732–1735, 2007.
Takahashi, T., Sutherland, S. C., Wanninkhof, R., Sweeney, C., Feely, R. A., Chipman, D. W., Hales, B., Friederich, G., Chavez, F., Sabine, C., Watson, A., Bakker, D. C., Schuster, U., Metzl, N., Yoshikawa-Inoue, H., Ishii, M., Midorikawa, T., Nojiri, Y., Körtzinger, A., Steinhoff, T., Hoppema, M., Olafsson, J., Arnarson, T. S., Tilbrook, B., Johannessen, T., Olsen, A., Bellerby, R., Wong, C., Delille, B., Bates, N., and de Baar, H. J.: Climatological mean and decadal change in surface ocean pCO_2, and net sea–air CO_2 flux over the global oceans, Deep-Sea Res. Pt. II, 56, 554–577, 2009.
Takigawa, M., Sudo, K., Akimoto, H., Kita, K., Takegawa, N., Kondo, Y., and Takahashi, M.: Estimation of the contribution of intercontinental transport during the PEACE campaign by using a global model, J. Geophys. Res., 110, D21313, doi:10.1029/2005JD006226, 2005.
Tiedtke, M.: A comprehensive mass flux scheme for cumulus parameterization in large-scale models, Mon. Weather Rev., 117, 1779–1800, 1989.
Tomita, H. and Satoh, M.: A new dynamical framework of nonhydrostatic global model using the icosahedral grid, Fluid Dyn. Res., 34, 357–400, 2004.
Xueref-Remy, I., Bousquet, P., Carouge, C., Rivier, L., Viovy, N., and Ciais, P.: Variability and budget of CO_2 in Europe: analysis of the CAATER airborne campaigns – Part 2: Comparison of CO_2 vertical variability and fluxes from observations and a modeling framework, Atmos.

ACPD
11, 12805–12848, 2011

Chem. Phys. Discuss., 10, 4271–4304, doi:10.5194/acpd-10-4271-2010, 2010.
Yang, Z., Washenfelder, R. A., Keppel-Aleks, G., Krakauer, N. Y., Randerson, J. T., Tans, P. P., Sweeney, C., and Wennberg, P. O.: New constraints on Northern Hemisphere growing season net flux, Geophys. Res. Lett., 34, L12807, doi:10.1029/2007GL029742, 2007.

ACPD
11, 12805–12848, 2011

Table 1. Aggregated non-fossil fuel carbon budget of flux data (unit is Pg C yr^{-1}). The definition of the regional aggregation is the same as that of TransCom3 (Gurney et al., 2004).

Region Name	Flux1	Flux2
Northern land	0.00	−1.38
Tropical land	0.00	1.35
Southern land	0.00	−0.72
Northern ocean	−1.00	−1.67
Tropical ocean	0.70	0.94
Southern ocean	−1.11	−1.32

ACPD
11, 12805–12848, 2011

Table 2. List of the CONTRAIL airports and data density. Numbers of flights are calculated by counting take-offs and landings over each airport. Latitude and longitude values are derived by averaging those of the measurement points during take-offs and landings.

City	Code	Latitude	Longitude	Number of flights		Region
				2006	2007	
Narita	NRT	35.60° N	140.36° E	411	1044	EAS
Osaka	KIX	34.54° N	135.15° E	60	205	EAS
Nagoya	NGO	35.22° N	136.89° E	74	172	EAS
Paris	CDG	49.92° N	3.41° E	52	107	EUR
Vancouver	YVR	49.10° N	123.91° W	44	115	WNA
Jakarta	CGK	5.42° S	107.26° E	41	106	SSA
Fukuoka	FUK	33.81° N	131.01° E	30	102	EAS
London	LHR	51.86° N	1.26° E	23	108	EUR
Incheon	ICN	37.15° N	127.51° E	32	72	EAS
Honolulu	HNL	21.55° N	158.92° W	27	75	HWI
Taipei	TPE	25.49° N	121.92° E	5	90	EAS
Bangkok	BKK	14.17° N	101.52° E	17	70	NSA
Delhi	DEL	28.20° N	77.95° E	18	66	IND
Singapore	SIN	1.89° N	104.42° E	34	47	SSA
Tokyo	HND	35.13° N	139.64° E	6	56	EAS
Pusan	PUS	35.16° N	129.83° E	33	22	EAS
Milan	MXP	46.09° N	9.46° E	28	20	EUR
Denpasar	DPS	8.01° S	115.36° E	2	44	SSA
Mexico City	MEX	19.92° N	99.48° W	9	32	SNA
Roma	FCO	42.76° N	12.48° E	16	24	EUR
Amsterdam	AMS	52.94° N	6.10° E	0	40	EUR

ACPD
11, 12805–12848, 2011

Table 2. Continued.

City	Code	Latitude	Longitude	Number of flights		Region
				2006	2007	
Sydney	SYD	33.14° S	150.88° E	13	26	AUS
Osaka	ITM	34.63° N	136.06° E	0	32	EAS
Moscow	SVO	56.87° N	37.88° E	8	18	EUR
Brisbane	BNE	26.54° S	152.64° E	0	22	AUS
Los Angeles	LAX	34.42° N	119.03° W	18	0	WNA
Chitose	CTS	42.06° N	141.62° E	2	8	EAS
Ulaanbaatar	ULN	47.46° N	107.31° E	4	2	EAS
Guam	GUM	14.27° N	144.56° E	4	2	NSA
Zurich	ZRH	48.55° N	8.95° E	4	0	EUR
Naha	OKA	26.46° N	128.04° E	2	2	EAS
Hiroshima	HIJ	34.79° N	133.76° E	0	4	EAS
Kuala Lumpur	KUL	2.82° N	102.62° E	2	0	SSA
Alice Springs	ASP	23.76° S	134.41° E	2	0	AUS
Las Vegas	LAS	36.45° N	116.06° W	2	0	WNA
Manila	MNL	14.78° N	121.60° E	0	2	NSA
Budapest	BUD	48.51° N	19.68° E	0	2	EUR
Iwakuni	IWJ	33.81° N	133.02° E	0	2	EAS
Sendai	SDJ	38.04° N	141.61° E	0	2	EAS

ACPD
11, 12805–12848, 2011

Table 3. Surface marine boundary layer sites of GLOBALVIEW.

Site name	Latitude	Longitude	Code
Storhofdi, Vestmannaeyjar	63.40° N	20.29° W	ice_01D0
Cold Bay, Alaska	55.21° N	162.72° W	cba_01D0
Shemya Island, Alaska	52.72° N	174.10° E	shm_01D0
Terceira Island, Azores	38.77° N	−27.38° W	azr_01D0
Sand Island, Midway	28.21° N	177.38° W	mid_01D0
Minamitorishima	24.30° N	153.97° E	mnm_19C0
Cape Kumukahi, Hawaii	19.52° N	154.82° W	kum_01D0
Mariana Islands, Guam	13.43° N	144.78° E	gmi_01D0
Christmas Island	1.70° N	157.17° W	chr_01D0
Tutuila, American Samoa	14.25° S	170.56° W	smo_01C0

ACPD
11, 12805–12848, 2011

Table 4. Seasonal amplitudes of the observed and the simulated seasonal mean variations at 5–6 km over each area for 2006–2007 and correlation coefficients between those seasonal variations. The seasonal amplitude is defined as the difference between the seasonal minimum and maximum.

Region	Seasonal amplitude			Correlation coefficient	
	Obs.	Flux1	Flux2	Flux1	Flux2
EAS	7.34	5.47	5.53	0.98	0.99
EUR	8.71	6.45	6.85	0.98	0.99
WNA	8.83	7.15	7.74	0.98	0.99
HWI	6.55	4.83	4.86	0.99	0.99
IND	7.61	4.23	4.12	0.96	0.94
NSA	4.36	3.05	3.15	0.91	0.91
SSA	2.01	1.07	1.30	0.90	0.83
SNA	9.17	4.64	4.56	0.94	0.96
AUS	2.86	1.19	2.12	0.93	0.88

ACPD
11, 12805–12848, 2011

Table 5. Ratios of seasonal amplitudes to that at 4–5 km in the northern area for 2007. Simulated results are derived using Flux2 and Flux1 (parenthetical values).

	Obs.	ACTM	MJ98-CDTM	NICAM-TM	NIES
N. MBL	1.51	1.43 (1.31)	1.69 (1.47)	1.40 (1.27)	1.37 (1.26)
EAS, EUR, WNA (7–8 km)	0.86	0.83 (0.81)	0.69 (0.73)	0.89 (0.88)	0.89 (0.89)

ACPD
11, 12805–12848, 2011

Table 6. Latitudinal difference of mean ΔCO_2 between north (20–70° N) and tropics (20° S–20° N) at 5–6 km in the free-troposphere (a) and in the marine boundary layer (MBL) (b). Simulated results are derived using Flux2 and Flux1 (parenthetical values).

(a) 5–6 km

	OBS	ACTM	MJ98-CDTM	NICAM-TM	NIES
JFM	1.90	2.15 (2.15)	1.29 (1.18)	2.20 (2.10)	2.21 (2.26)
JAS	−1.83	−1.14 (−0.30)	−0.83 (−0.24)	−1.37 (−0.83)	−0.75 (0.01)
Annual mean	0.56	0.86 (1.48)	0.62 (0.98)	0.92 (1.27)	1.07 (1.68)

(b) MBL

	OBS	ACTM	MJ98-CDTM	NICAM-TM	NIES
JFM	3.88	3.73 (4.10)	1.21 (1.12)	3.89 (4.13)	2.83 (3.07)
JAS	−4.70	−3.72 (−1.85)	−4.19 (−2.26)	−3.98 (−1.76)	−2.66 (−1.09)
Annual mean	0.82	1.09 (2.24)	−0.52 (0.38)	1.00 (2.07)	0.97 (1.87)

ACPD
11, 12805–12848, 2011

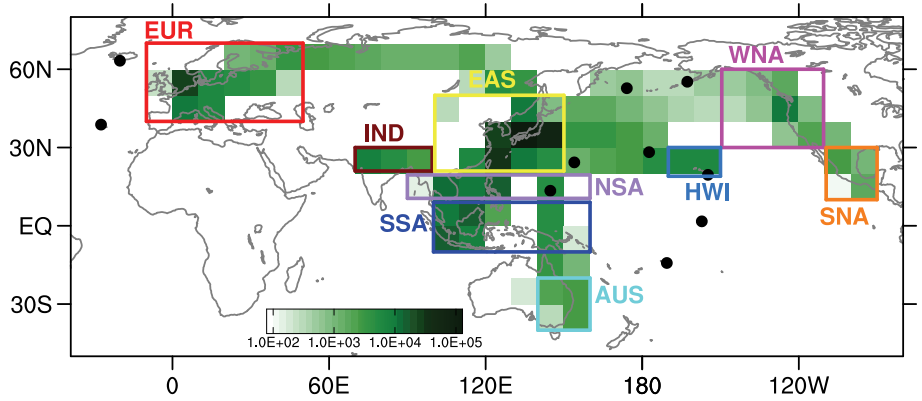

Fig. 1. Number of data in each latitude–longitude grid (10° × 10°) (green shaded) and area distinctions used for the analyses in this study: Europe (EUR: 40–70° N, 10° W–50° E), western North America (WNA: 30–60° N, 110–150° W), East Asia (EAS: 20–50° N, 100–150° E), Hawaii (HWI: 20–30° N, 150–170° W), southern North America (SNA: 10–30° N, 90–110° W), Indian continent (IND: 20–30° N, 70–100° E), northern Southeast Asia (NSA: 10–20° N, 90–160° E), southern Southeast Asia (SSA: 10° S–10° N, 100–160° E) and Australia (AUS: 20–40° S, 140–160° E). Details of airport locations are presented in Table 2. Solid black circles denote locations of GLOBALVIEW marine boundary layer sites.

ACPD
11, 12805–12848, 2011

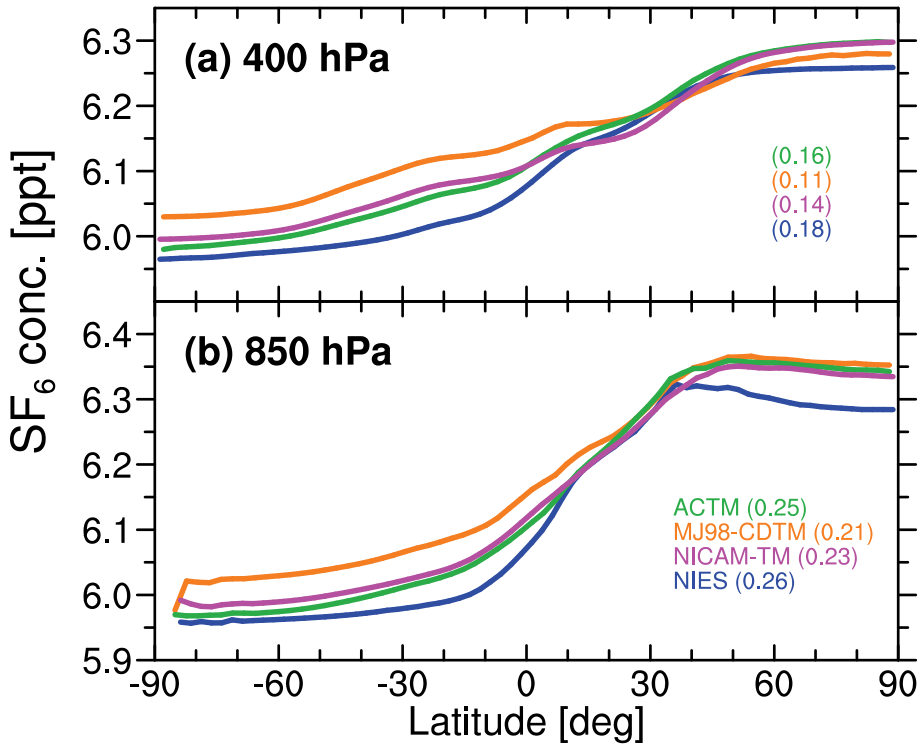

Fig. 2. Latitudinal distributions of annual zonal mean of SF_6 concentrations at 400 hPa **(a)** and 850 hPa **(b)**, simulated by ACTM (green), MJ98-CDTM (orange), NICAM-TM (magenta), and NIES (blue). Parenthetical values represent differences of area-weighted mean SF_6 concentrations between in the Northern and Southern Hemispheres. The global constant offset of 4.7 ppt is added to the simulation results according to the estimate by ESRL/NOAA for the global average at the beginning of the simulation.

ACPD
11, 12805–12848, 2011

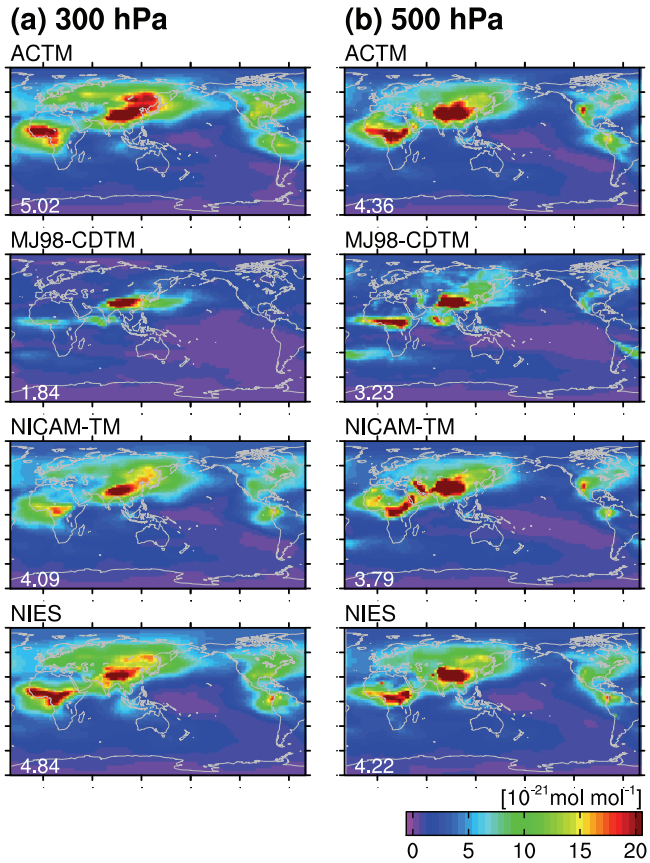

Fig. 3. Longitude–latitude distributions of radon concentrations at 300 hPa **(a)** and 500 hPa **(b)** for June–July–August (JJA) of 2007 simulated by the models: ACTM (uppermost panels), MJ98-CDTM (middle upper panels), NICAM-TM (middle lower panels), and NIES (lowest panels). Values at the lower left corner in panels are the global average of radon mole fraction (10^{-21} mol mol^{-1}).

ACPD
11, 12805–12848, 2011

Three-dimensional variations of atmospheric CO_2

Y. Niwa et al.

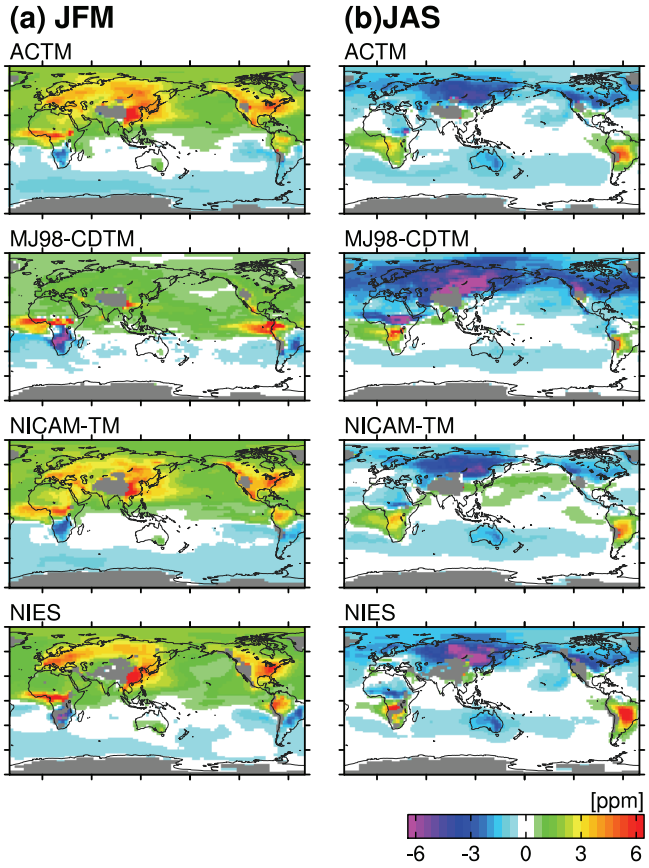

Fig. 4. Seasonal mean vertical difference of CO_2 between 850 hPa and 500 hPa for JFM **(a)** and JAS **(b)** of 2007, simulated by ACTM (uppermost panels), MJ98-CDTM (middle upper panels), NICAM-TM (middle lower panels), and NIES (lowest panels). Positive values mean that the CO_2 concentration at 850 hPa is larger than that at 500 hPa.

ACPD
11, 12805–12848, 2011

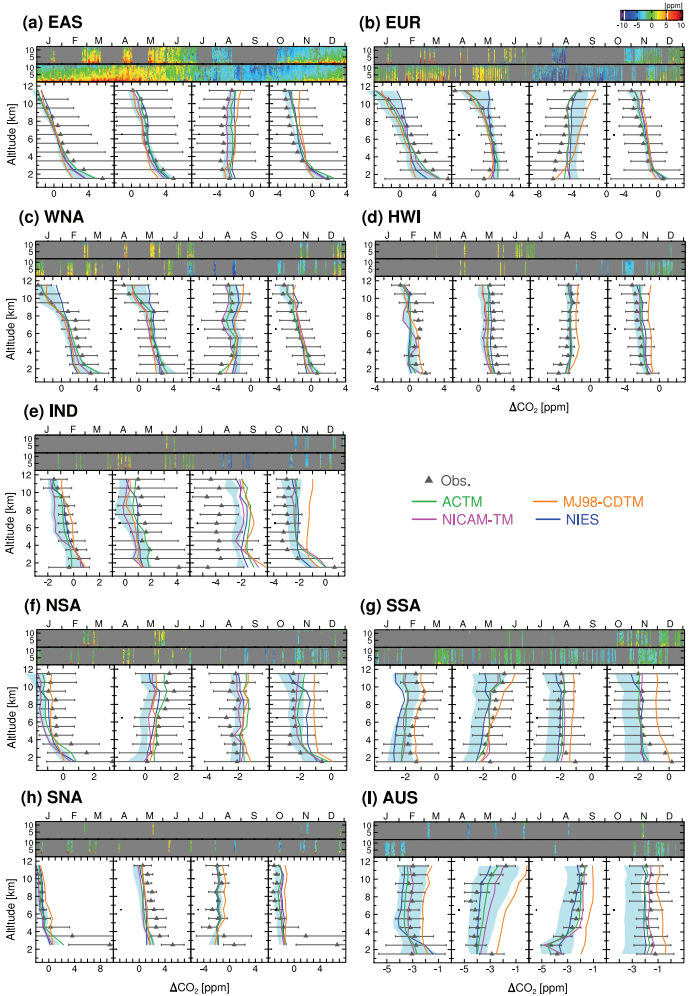

Fig. 5. Caption on next page.

ACPD
11, 12805–12848, 2011

Three-dimensional variations of atmospheric CO_2

Y. Niwa et al.

Fig. 5. Seasonal mean vertical profiles over each area for 2006–2007. Lines are simulated results from Flux2: ACTM (green), MJ98-CDTM (orange), NICAM-TM (magenta) and NIES (blue). Cyan shading shows the range of the simulated results obtained using Flux1. Gray triangles show data derived from CONTRAIL. The error bar shows the mean standard deviation. Vertical profiles are seasonally averaged for January–February–March (JFM), April–May–June (AMJ), July–August–September (JAS), and October–November–December (OND). The top two panels in each figure show time–altitude cross-section of daily ΔCO_2 from the CONTRAIL data for 2006 (upper panel) and 2007 (lower panel).

ACPD
11, 12805–12848, 2011

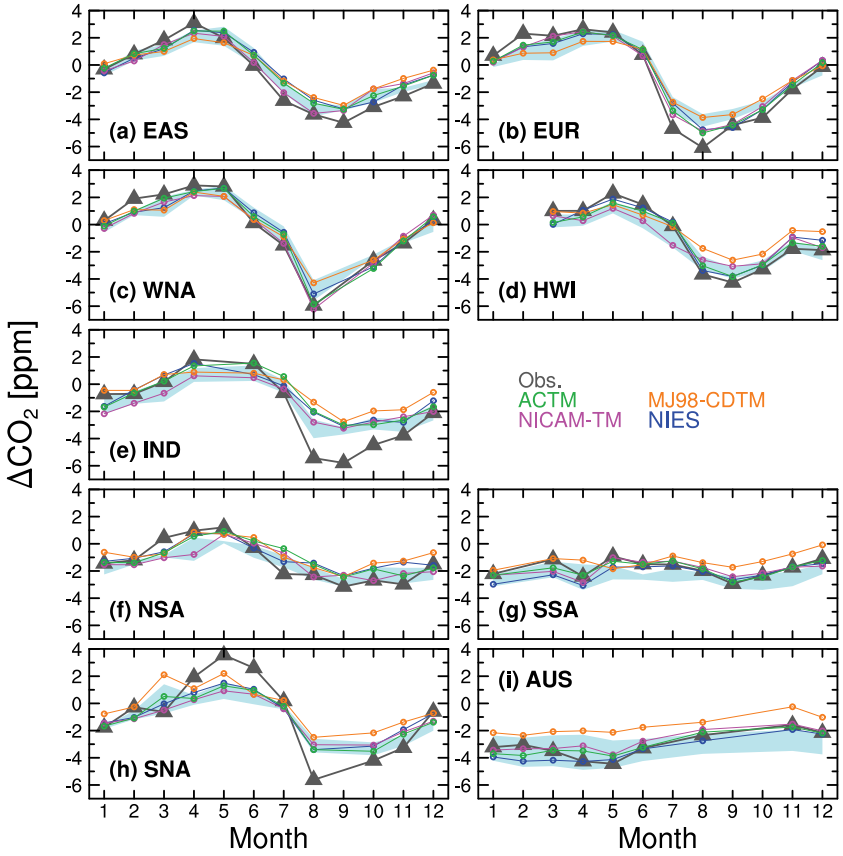

Fig. 6. Seasonal mean variations of ΔCO_2 at 5–6 km over each area for 2006–2007. Gray triangles with lines show data derived from CONTRAIL. Circles with lines are simulated results from Flux2: ACTM (green), MJ98-CDTM (orange), NICAM-TM (magenta), and NIES (blue). Cyan shade shows range of the simulated results from Flux1.

ACPD
11, 12805–12848, 2011

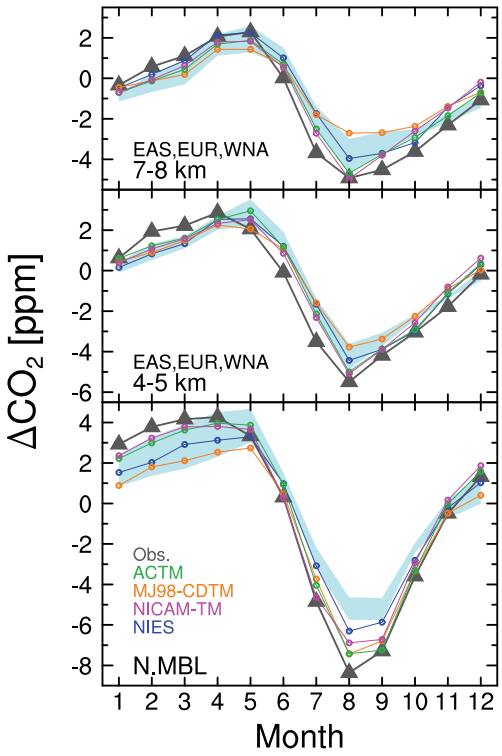

Fig. 7. Seasonal mean variations of ΔCO_2 in the northern area for 2007. Data are averages of seasonal variations at six marine boundary layer (MBL) sites located between 20° N and 70° N for N. MBL (lowest panel) and at 4–5 km (middle panel) and 7–8 km (uppermost panel) over the northern area, as aggregated from East Asia (EAS), Europe (EUR) and western North America (WNA). Gray triangles with lines show data derived from CONTRAIL/GLOBALVIEW. Circles with lines are simulated results from Flux2: ACTM (green), MJ98-CDTM (orange), NICAM-TM (magenta), and NIES (blue). Cyan shade shows range of the simulated results from Flux1.

ACPD
11, 12805–12848, 2011

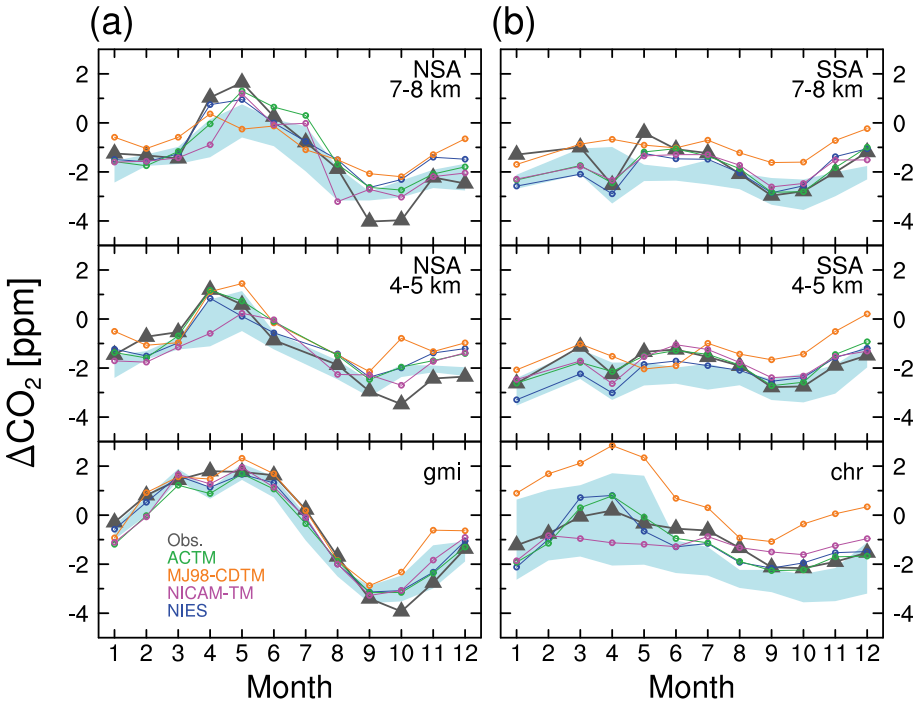

Fig. 8. Seasonal mean variations of ΔCO_2 over the northern and southern Southeast Asia areas (NSA **(a)**, SSA **(b)**), and at MBL sites latitudinally near each tropical area (gmi, chr) for 2007. Gray triangles with lines show data derived from CONTRAIL/GLOBALVIEW. Open circles with lines are simulated results from Flux2: ACTM (green), MJ98-CDTM (orange), NICAM-TM (magenta), and NIES (blue). Cyan shade shows range of the simulated results from Flux1.

ACPD
11, 12805–12848, 2011

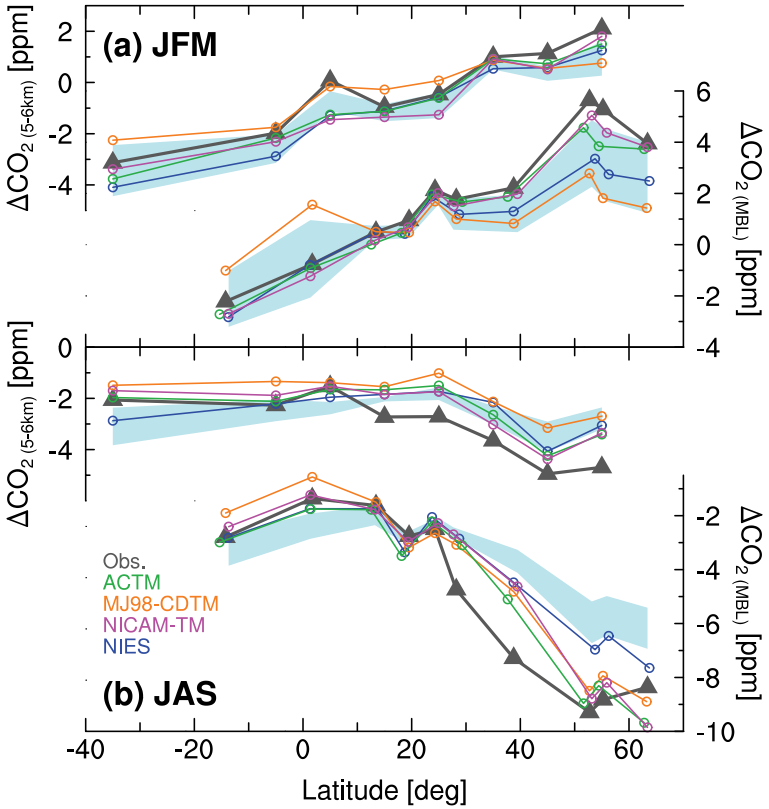

Fig. 9. Latitudinal mean profile of ΔCO_2 at 5–6 km in the free-troposphere (upper) and at the marine boundary layer (MBL) sites (lower) for January–February–March (JFM) **(a)** and July–August–September (JAS) **(b)** of 2007. Gray triangles with lines show the observed data from CONTRAIL. Open circles with lines show simulated results from Flux2: green (ACTM), orange (MJ98-CDTM), magenta (NICAM-TM), and blue (NIES). Cyan shade shows the range of the simulated results from Flux1.

ACPD
11, 12805–12848, 2011